JOURNAL OF SPACECRAFT AND ROCKETS
Vol. 44, No. 6, November–December 2007

Drag Sail for End-of-Life Disposal from Low Earth Orbit

Peter C. E. Roberts* and Patrick G. Harkness†
Cranfield University,
Cranfield, Bedfordshire, MK43 0AL England, United Kingdom

DOI: 10.2514/1.28626

International standards are moving toward the requirement that spacecraft should be removed from orbit at the end of their operational lives. The feasibility of a deployable aerodynamically stable drag-enhancement structure is considered for the end-of-life disposal of low-Earth-orbit spacecraft, and how this structure could fulfill NASA deorbit guidelines is demonstrated. The concept is a thin membrane supported by deployed struts. A shuttlecocklike geometry is chosen to take advantage of the small stabilizing effect caused by oscillatory motion in, and descent through, the free molecular flow during deorbit. The shuttlecock is approximated to a cone, and the aerodynamic loads due to orbital and rotational motion are calculated and used to model the stabilization and descent of a deployed system toward final reentry. Finally, it is shown that this system can provide an effective and mass-efficient deorbit solution for future missions.

Nomenclature

A	=	area
F_{BD}	=	aerodynamic drag force in body axes
F_{BL}	=	aerodynamic lift force in body axes
F_n	=	aerodynamic force normal to surface of the idealized conical deorbit device
M	=	aerodynamic moment about the apex of the idealized conical deorbit device
S	=	slant height of the idealized conical deorbit device
T_D	=	aerodynamic damping torque about the apex of the idealized conical deorbit device
T_R	=	aerodynamic restoring torque about the apex of the idealized conical deorbit device
V	=	velocity of the idealized conical deorbit device through the free molecular flow
V_n	=	component of flow velocity normal to the surface of the idealized conical deorbit device
l	=	overall height of the idealized conical deorbit device
r	=	radius of the idealized conical deorbit device
s	=	linear distance from the apex along the slant height of the idealized conical deorbit device
α	=	angle of attack of the idealized conical deorbit device
θ	=	apex half-angle of the idealized conical deorbit device
λ	=	radial limit of flow impingement on the idealized conical deorbit device (as a fraction of S)
ρ	=	atmospheric density
ϕ	=	circumferential angle around the idealized conical deorbit device
ϕ_L	=	circumferential limit of flow impingement on the idealized conical deorbit device

I. Introduction

SEVERAL international standards require that spacecraft be removed from orbit at the end of their operational lives (EOLs). For low-Earth-orbit (LEO) spacecraft, the present NASA deorbit guideline [1] simply states that postmission orbital lifetime should not exceed 25 years, but every likelihood exists that this time limit will be reduced in the future.

By encouraging the rapid removal of large objects from LEO, these guidelines help to reduce the amount of hazardous debris in orbit, not only in terms of gross tonnage, but also in terms of the number of fragments that the spacecraft could otherwise spall into space. Spontaneous fragmentation of defunct objects, caused by either internal explosions or in-orbit collisions, has produced approximately 3600 of around 9400 objects currently being tracked in LEO [2].

For a LEO spacecraft to deorbit effectively has hitherto required a deliberate maneuver carried out from a controlled platform, such as a deorbit burn or tether deployment. However, this implies that the spacecraft is not truly at the end of life, but is rather being deorbited while the capacity to do so remains intact and could be at odds with maximizing the return on investment.

An alternative solution would be to carry a standardized lightweight deorbit package that could remove spacecraft from orbit at the EOL even if the spacecraft had suffered a failure that left it inactive or unmaneuverable. Such a system could take the form of a limpetlike package that would be attached to new spacecraft before launch. At the true end of life, a signal from the ground would trigger the device, which would respond by deploying an aerostable shuttlecocklike drag sail. This would remove energy from the orbit of the host, greatly accelerating the decay of its orbit.

It is upon the design and optimization of such a system that this work concentrates. We shall consider first the advantages unique to our system and then develop an analytic model to estimate the aerodynamic forces that may reasonably be generated. We will then combine these forces with an attitude and orbit propagator and analyze the performance of a range of drag sails under different deployment conditions. This process will allow us to draw conclusions regarding the optimal shape and deployment conditions of the drag sail itself. Although proof of concept is only shown for equatorial orbits, the same design should be applicable to the full range of inclinations.

II. Drag Enhancement as a Deorbit Mechanism

Previous researchers [3,4] have discussed a variety of methods for the EOL disposal of spacecraft in LEO. These methods can be summarized into three areas: namely, tethers, thrusters, and drag enhancement. Ideally, the solution should be independent of the spacecraft itself, because the failure event may produce an uncontrolled tumbling motion, making the useful firing of thrusters or deployment of tethers difficult. This consideration makes the deployment of an aerostable drag-enhancement device the most robust option for the disposal of LEO spacecraft.

Received 30 October 2006; revision received 30 March 2007; accepted for publication 10 May 2007. Copyright © 2007 by Cranfield University. Published by the American Institute of Aeronautics and Astronautics, Inc., with permission. Copies of this paper may be made for personal or internal use, on condition that the copier pay the $10.00 per-copy fee to the Copyright Clearance Center, Inc., 222 Rosewood Drive, Danvers, MA 01923; include the code 0022-4650/07 $10.00 in correspondence with the CCC.

*Lecturer, Space Research Centre.
†Ph.D. Student, Space Research Centre.

Drag enhancement is specifically considered by the aforementioned NASA guideline [1], which states that

> If drag-enhancement devices are to be used to reduce the orbit lifetime, it should be demonstrated that such devices will significantly reduce the area-time product of the system or will not cause the spacecraft or large debris to fragment if a collision occurs while the system is decaying from orbit.

To determine if this condition is met, we must first concede that a deployed drag-enhancement device will reduce the remaining orbital lifetime by reducing the mass-to-area ratio (kg/m^2) but leaving the area-time product largely unaffected; we further concede that given a constant debris population, the number of in-orbit collisions will also remain largely unchanged. Nevertheless, it can be shown that the risk of a collision actually resulting in a fragmentation event is greatly reduced, because if a large drag sail is deployed, the impacts will be distributed across the entire drag area, rather than concentrated onto the spacecraft bus itself. Because the drag sail will be a gossamer structure that can be punctured by, but will not fragment, incoming debris objects, the majority of impacts upon the system will not result in the production of substantial secondary debris particles. Furthermore, the debris population is currently growing. To sweep the area-time volume in a period of (relatively) low debris density will result in fewer impacts than if that volume were extended into the increasingly dense debris environment of the future.

Meyer and Chao [3] calculated that drag enhancement is the most mass-efficient method for the 25-year deorbit of a dense satellite orbiting below 900 km, although Petro [5] suggested a more conservative value of 700 km, and Campbell [6] believed that the system may be applicable up to 1000 km. In all three cases, it was assumed that the required drag enhancement was achieved by the deployment of an inflatable balloon. It seems clear then that the NASA guideline in LEO can be fulfilled by a drag-enhancement mechanism up to an altitude of around 700–1000 km, not by reducing the area-time product, but by reducing the production of secondary debris created during the deorbit procedure.

III. Rarefied-Flow Aerodynamics

To determine the best shape for the deployed sail during the stabilization and deorbit phases of operation, we must first calculate the aerodynamic loads exerted upon it by the rarefied free molecular flow in LEO.

Although a drag sail supported between radial struts will be pyramidal in shape, approximating that shape to a cone eases the analytical evaluation of those loads by introducing rotational symmetry and reducing the number of individual surfaces that must be considered to one.

The normal velocity of freestream flow impingement onto the idealized conical surface as a fraction of the orbital velocity is a function of α, θ, and ϕ, where α defines the deviation of the idealized cone from stable alignment with the flow vector in any plane, θ is the apex half-angle of the cone, and ϕ is a circumferential angle that is equal to zero on the X–Z body-axis plane for negative Z and that increases clockwise around the surface, as viewed from the apex. Thus, zero ϕ is near the top in Figs. 1a and 1b.

By spherical trigonometry, the normal impingement velocity on the surface of the cone may be found by Eq. (1).

$$V_n = V(\sin\theta\cos\alpha - \cos\phi\cos\theta\sin\alpha) \tag{1}$$

A. Flow Regimes

However, normal impingement is impossible in those regions that are shielded from the oncoming flow vector by another part of the cone. These lee regions migrate across the structure with variations in angle of attack, but their behavior can be simplified if one considers them in the context of four regimes, as illustrated in Fig. 1.

1. Flow Regime 1

In regime 1, the angle of attack is less than θ and the entire internal surface of the cone is a lee region.

2. Flow Regime 2

In regime 2, the angle of attack is greater than θ but less than $\pi/2$. Under these conditions, the entire internal surface of the cone remains a lee region, but a section of the external surface becomes one as well. The limit of the external lee region is quantified in terms of the circumferential coordinate ϕ, with flow vector impingement impossible in the region in which ϕ is less than a limiting value ϕ_L.

The value of ϕ_L can calculated by setting Eq. (1) to zero, implying zero-normal impingement velocity; which results in Eq. (2).

$$\phi_L = \cos^{-1}(\tan\theta\cot\alpha) \tag{2}$$

3. Flow Regime 3

In regime 3, the angle of attack is greater than $\pi/2$ but does not exceed $\pi - \theta$. The external lee region continues to be governed by Eq. (2), but the situation is complicated by the impingement of the flow vector upon the internal surface of the cone.

As was set out earlier, the external lee region persists when $\phi < \phi_L$. Therefore, the internal lee region is now limited to the region in which $\phi > \phi_L$, simply because an otherwise-unimpeded flow can always impinge on one side or the other of a locally flat surface.

However, the flow is not unimpeded. The external windward lip of the cone prevents impingement nearer the apex on the internal leeward side, as illustrated in Figs. 2 and 3. This additional lee can be quantified in terms of the lee fraction λ, which varies from zero at the apex to one at the lip of the cone.

To begin the calculation of λ, Fig. 2 shows the cone, complete with parameters as yet unused, from an angle perpendicular to the flow vector, and Fig. 3 considers the system from the point of view of the flow vector itself. It becomes obvious that λ is a function of the circumferential angle ϕ.

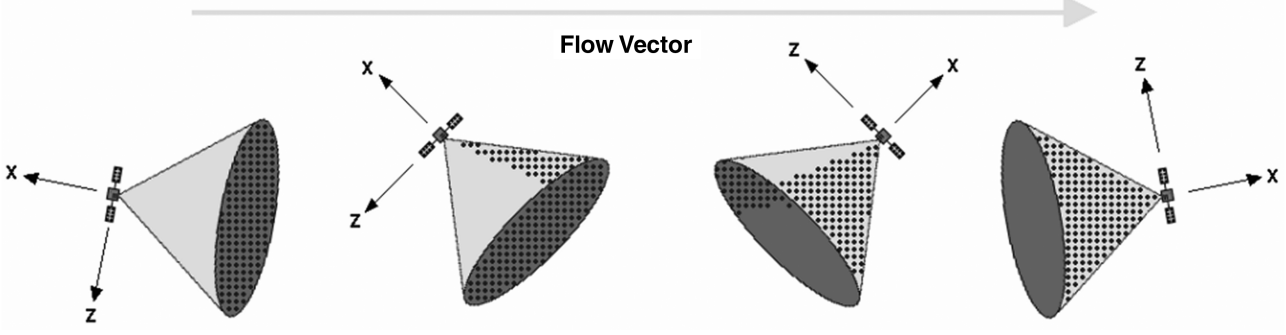

a) Regime 1 b) Regime 2 c) Regime 3 d) Regime 4

Fig. 1 The surface experiences a flow vector, as shown by the arrow, but this vector cannot impinge upon the lee regions, indicated by dots; the three transitions occur at $\alpha = \theta$, $\alpha = \pi/2$, and $\alpha = \pi - \theta$.

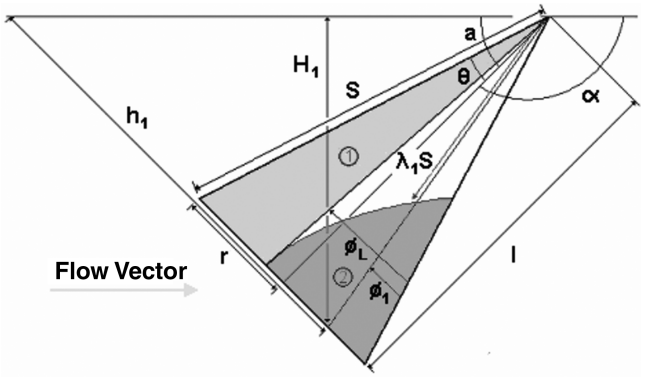

Fig. 2 Illustration of the regions of external impingement (1) and internal impingement (2) that exist in flow regime 3; the flow vector is denoted by the arrow, and it should be noted that ϕ_1 and ϕ_L are angular measurements around the curved surface.

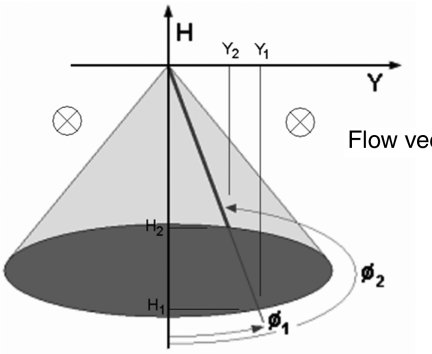

Fig. 3 A cone in regime 3 viewed from the point of view of the freestream flow vector.

To determine the exact variation of λ with ϕ, the proportion of the strip at ϕ_1 that lies beneath another strip at the subtended angle ϕ_2 must be calculated. To achieve this, the length of the line h_1 in Fig. 2 must be determined from the geometry of the cone.

$$h_1 = l\tan a + r\cos\phi_1 \tag{3}$$

The projection of h_1 as H_1 onto the Y–H plane can be obtained and expressed as Eq. (4). The negative sign reflects the convention of H being positive upward, whereas Y_1, as defined in Fig. 3, is expressed by Eq. (5).

$$H_1 = -\cos a(l\tan a + r\cos\phi_1) \tag{4}$$

$$Y_1 = r\sin\phi_1 \tag{5}$$

The diagonal line in Fig. 3 represents a strip at ϕ_1 that when projected onto the Y–H plane is also the hypotenuse of a right-angled triangle for which the other sides are Y_1 and H_1. This projected line has a gradient G_1 on the Y–H plane.

$$G_1 = \frac{H_1}{Y_1} \tag{6}$$

However, ϕ_1 and ϕ_2 occlude on the Y–H plane and so $G_1 = G_2 = G$.

Substituting H_1 and Y_1 back into Eq. (6) and rearranging gives a quadratic equation.

$$G\sin\phi_1 + \cos a(\cos\phi_1) = \frac{-l\sin a}{r} \tag{7}$$

Noting that ϕ_1 can be exchanged for ϕ_2 in Eq. (7), and after further substitution and rearrangement, the quadratic solution in ϕ_1 and ϕ_2 may be given by Eq. (8).

$$\phi_1, \phi_2 = \cos^{-1}\left[\frac{-l\sin 2a}{2r(G^2+\cos^2 a)} \pm \frac{G}{G^2+\cos^2 a}\left(G^2+\cos^2 a - \frac{l^2\sin^2 a}{r^2}\right)^{\frac{1}{2}}\right] \tag{8}$$

The fraction of the strip at ϕ_1 in the lee of the strip at ϕ_2 will be equal to the fraction Y_2 is of Y_1. This is, by definition, equal to the lee fraction λ and, with reference to Eq. (5), can be written in terms of ϕ_2 and ϕ_1.

$$\lambda = \frac{\sin\phi_2}{\sin\phi_1} \tag{9}$$

Thus, the lee region on the inside of the cone is limited in ϕ to the condition $\phi < \phi_L$ and is limited in s to the condition $s < \lambda S$, where S is the slant height of the cone and λ is the solution of Eq. (9).

4. Flow Regime 4

In regime 4, the angle of attack is greater than $\pi - \theta$ and the entire external surface of the cone is a lee region.

B. Evaluation of Aerodynamic Forces and Torques

Given the normal impingement velocity and the zones in which that impingement occurs, the aerodynamic forces and torques acting upon the deployed drag sail can now be calculated.

However, before this can be carried out, the normal velocity expressed by Eq. (1) must be refined to account for the small aerodynamic damping torque. Because it is assumed that all of the mass of the system is concentrated in the apex (as would be the case if a gossamer structure were deployed from a much more massive host satellite), all rotations can be considered to take place about the apex as well. Equation (1) can therefore be revised to the form given in Eq. (10), with the inclusion of an additional term proportional to $\dot{\alpha}$ and the distance between the apex and the local point.

$$V_n = V(\sin\theta\cos\alpha - \cos\phi\cos\theta\sin\alpha) - s\dot{\alpha}\cos\phi \tag{10}$$

If one considers the force $\mathrm{d}F_n$ exerted on an annular element of area $\mathrm{d}A$, where

$$\mathrm{d}A = r\,\mathrm{d}\phi\,\mathrm{d}s = s\sin\theta\,\mathrm{d}\phi\,\mathrm{d}s \tag{11}$$

then, assuming the impinging free-molecular-flow particles lose all normal velocity, the normal force exerted on the conical surface may be estimated by Eq. (12). The multiplier of two reflects the symmetry that allows the integral to cover only half of the conical surface (i.e., the range $0 \le \phi \le \pi$).

$$F_n = 2\rho\sin\theta\int_0^S s\int_0^\pi [V(\sin\theta\cos\alpha - \cos\phi\cos\theta\sin\alpha) - s\dot{\alpha}\cos\phi]^2\,\mathrm{d}\phi\,\mathrm{d}s \tag{12}$$

This normal force is the basis for all of the aerodynamic forces and torques on the idealized cone. The drag force (in body axes) may be calculated by simply resolving the normal force through the apex half-angle, as in Eq. (13).

$$F_{\mathrm{BD}} = 2\rho\sin^2\theta\int_0^S s\int_0^\pi [V(\sin\theta\cos\alpha - \cos\phi\cos\theta\sin\alpha) - s\dot{\alpha}\cos\phi]^2\,\mathrm{d}\phi\,\mathrm{d}s \tag{13}$$

The aerodynamic lift (in body axes) may similarly be calculated, with a multiplier of $\cos\phi$ inserted to allow for the rotation of the normal force around the curved surface of the cone.

Table 1 Limits of integration for the expressions given by Eqs. (18–21)

Limits of integration for Eqs. (18–21)[a]	C	D	E	F
Regime 1	0	S	0	π
Regime 2	0	S	ϕ_L	π
Regime 3 (external contribution)	0	S	ϕ_L	π
Regime 3 (internal contribution)	λS	S	0	ϕ_L
Regime 4	0	S	0	π

[a]In Regimes 1, 2, and 4, the solutions can be calculated immediately. In Regime 3, the contributions from the external and internal flow impingement must be calculated separately and then summed.

$$F_{\mathrm{BL}} = 2\rho \sin\theta \cos\theta \int_0^S s \int_0^\pi [V(\sin\theta\cos\alpha - \cos\phi\cos\theta\sin\alpha) - s\dot{\alpha}\cos\phi]^2 \cos\phi \,\mathrm{d}\phi \,\mathrm{d}s \tag{14}$$

Multiplying the normal aerodynamic force by $\cos\phi$ and the local moment arm s yields a moment about the apex, as described by Eq. (15).

$$M = 2\rho \sin\theta \int_0^S s^2 \int_0^\pi [V(\sin\theta\cos\alpha - \cos\phi\cos\theta\sin\alpha) - s\dot{\alpha}\cos\phi]^2 \cos\phi \,\mathrm{d}\phi \,\mathrm{d}s \tag{15}$$

Separating the contributions due to α and $\dot{\alpha}$ in the preceding equation has the effect of separating the restoring torque and damping torque, T_R and T_D. These are expressed individually by Eqs. (16) and (17), with the small nonlinear terms in $\dot{\alpha}^2$ neglected.

$$T_R = 2\rho \sin\theta \int_0^S s^2 \,\mathrm{d}s \int_0^\pi [V(\sin\theta\cos\alpha - \cos\phi\cos\theta\sin\alpha)]^2 \cos\phi \,\mathrm{d}\phi \tag{16}$$

$$T_D = -4\rho \sin\theta \int_0^S s^3 \,\mathrm{d}s \int_0^\pi V(\sin\theta\cos\alpha - \cos\phi\cos\theta\sin\alpha)\dot{\alpha}\cos^2\phi \,\mathrm{d}\phi \tag{17}$$

Thus, expressions for the drag force, lift force, restoring torque, and damping torque can be expressed by Eqs. (18–21), with the limits of integration (given in Table 1) adjusted to account for the lee regions. The effect of $\dot{\alpha}$ was neglected for all but the aerodynamic damping equation, and the algebraic substitutions

$$A = \sin\theta\cos\alpha \quad \text{and} \quad B = \cos\theta\sin\alpha$$

were employed to simplify the expressions.

$$F_{\mathrm{BD}} = 2\rho\sin^2\theta \int_C^D s \,\mathrm{d}s \int_E^F [V(A - B\cos\phi)]^2 \,\mathrm{d}\phi \,\mathrm{d}s \tag{18}$$

$$F_{\mathrm{BL}} = 2\rho \sin\theta\cos\theta \int_C^D s \,\mathrm{d}s \int_E^F [V(A - B\cos\phi)]^2 \cos\phi \,\mathrm{d}\phi \,\mathrm{d}s \tag{19}$$

$$T_R = 2\rho \sin\theta \int_C^D s^2 \,\mathrm{d}s \int_E^F [V(A - B\cos\phi)]^2 \cos\phi \,\mathrm{d}\phi \tag{20}$$

$$T_D = -4\rho \sin\theta \int_C^D s^3 \,\mathrm{d}s \int_E^F V(A - B\cos\phi)\dot{\alpha}\cos^2\phi \,\mathrm{d}\phi \tag{21}$$

Equations (18–21) show that the lift, drag, and restoring torque are multiples of the square of the orbital velocity and atmospheric density (ρV^2), whereas the damping torque is a multiple of orbital velocity, atmospheric density, and pitch rate ($\rho V\dot{\alpha}$). Because these factors will change continuously during deorbit, the solutions can be divided by these parameter sets to render them universally applicable. The remainders after this division have been called aerodynamic quotients.

The aerodynamic quotients allow a range of equivalent cones (each with a surface area of 10 m^2, but an apex half-angle varying from 1.05 to 1.55 rad) to be compared. The drag, lift, restoring, and damping quotients of such a range will be as given in Figs. 4a–4d, respectively.

IV. Dynamic Simulation of the Deorbiting System

The next step in the optimization of the system is using these aerodynamic influences to propagate the behavior of a range of idealized spacecraft attached to a range of idealized drag sails, to determine the optimal drag sail and deployment conditions.

Because this investigation is limited to the equatorial plane, a 2-D space with the Earth at its center was used to model the performance

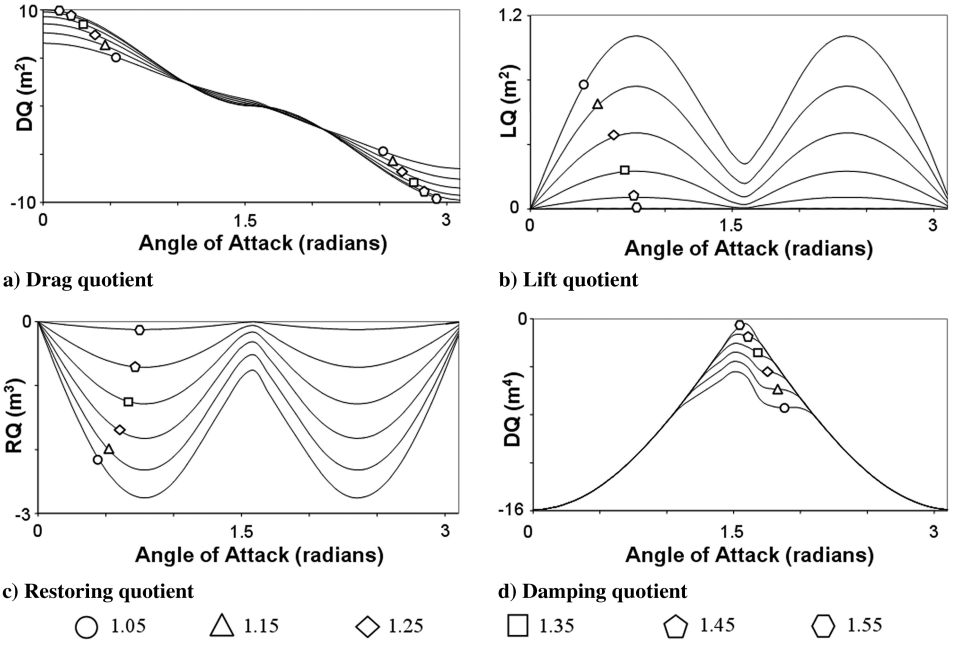

Fig. 4 Range of equivalent cones across all angles of attack.

of a range of deorbiting spacecraft with differing drag sails. Each system was given an initial circular velocity in the 2-D space and its subsequent motion propagated (using Newtonian mechanics written into a Simulink framework) under the influence of aerodynamic forces and torques (calculated by combining the preceding quotients with an MSIS-90 atmospheric density model [7]) and gravitational attraction (calculated from an inverse-square altitude relationship). The model begins each simulation in January of the fourth year of a typical solar cycle and outputs results such as the angle-of-attack history and the total time to deorbit, which is assumed to occur when the altitude first falls to 200 km, because rapid deorbit occurs below this altitude.

Solar radiation pressure (SRP) and gravity gradient torques were neglected, because the destabilizing effect of the SRP can be negated by the use of transparent sail material and the gravity gradient torque can be controlled by careful positioning of the device upon the much more massive host spacecraft (for a 50-m^2 sail at 400-km altitude, the gravity gradient perturbations are some two orders of magnitude less significant than the aerodynamic torques). In the latter case for the flatter sail geometries considered, any residual perturbation due to gravity torques will tend to aid stabilization.

The apex half-angle of each of the drag sails considered range through $1.07 \leq \theta \leq 1.56$ rad ($61 \leq \theta \leq 89$ deg), with increments of 0.01 rad. The initial angle of attack was similarly considered throughout the range $0 \leq \alpha \leq 3$ rad ($0 \leq \alpha \leq 172$ deg), with increments of 0.25 rad and an initial rate of one revolution per orbit in the Earth-centered inertial frame. The initial hour angle (i.e., the local time at the moment of deployment) was considered at 0000, 0600, 1200, and 1800 hrs, whereas the initial altitude was considered at 450, 550, and 650 km. Finally, drag sails of 10, 30, 90, 270, and 810 m^2 attached to host spacecraft of 10, 30, 90, 270, and 810 kg, respectively, were considered, maintaining a deployed mass-to-area ratio of 1 kg/m^2. These simulation sets amount to some 39,000 unique deorbit scenarios, throughout which the host spacecraft is held as a solid uniform sphere with a mass density of 760 kg/m^3.

It should be noted at this point that no precessional or rolling motions are considered to simplify the resulting data set. High initial angular rates will tend to average the drag area to the flow and will increase the deorbit time relative to the case in which the sail is stabilized into the flow.

V. Results of the Deorbit Simulations

Deorbit times from 450 km are shown in Fig. 5. Deorbit times from 550 km are shown in Fig. 6. Deorbit times from 650 km are shown in Fig. 7. Typical angle-of-attack histories are shown in Fig. 8.

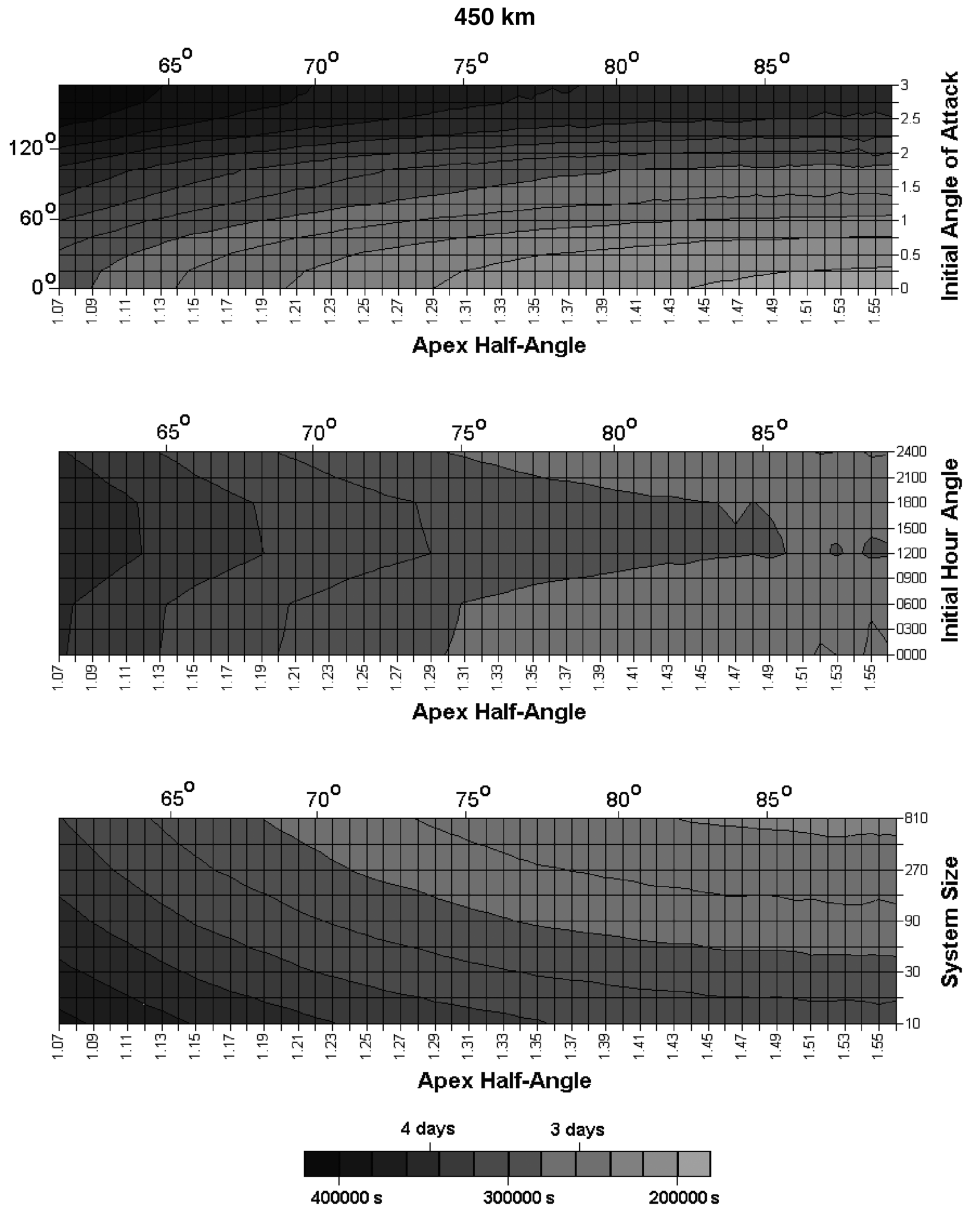

Fig. 5 Average deorbit times (see scale bar) from 450 km, varying with apex half-angle (in radians), initial angle of attack (in radians), initial hour angle (in hours), and system size (in kg and m^2); mass-to-area ratio is reduced by the drag sail to 1 kg/m^2 throughout.

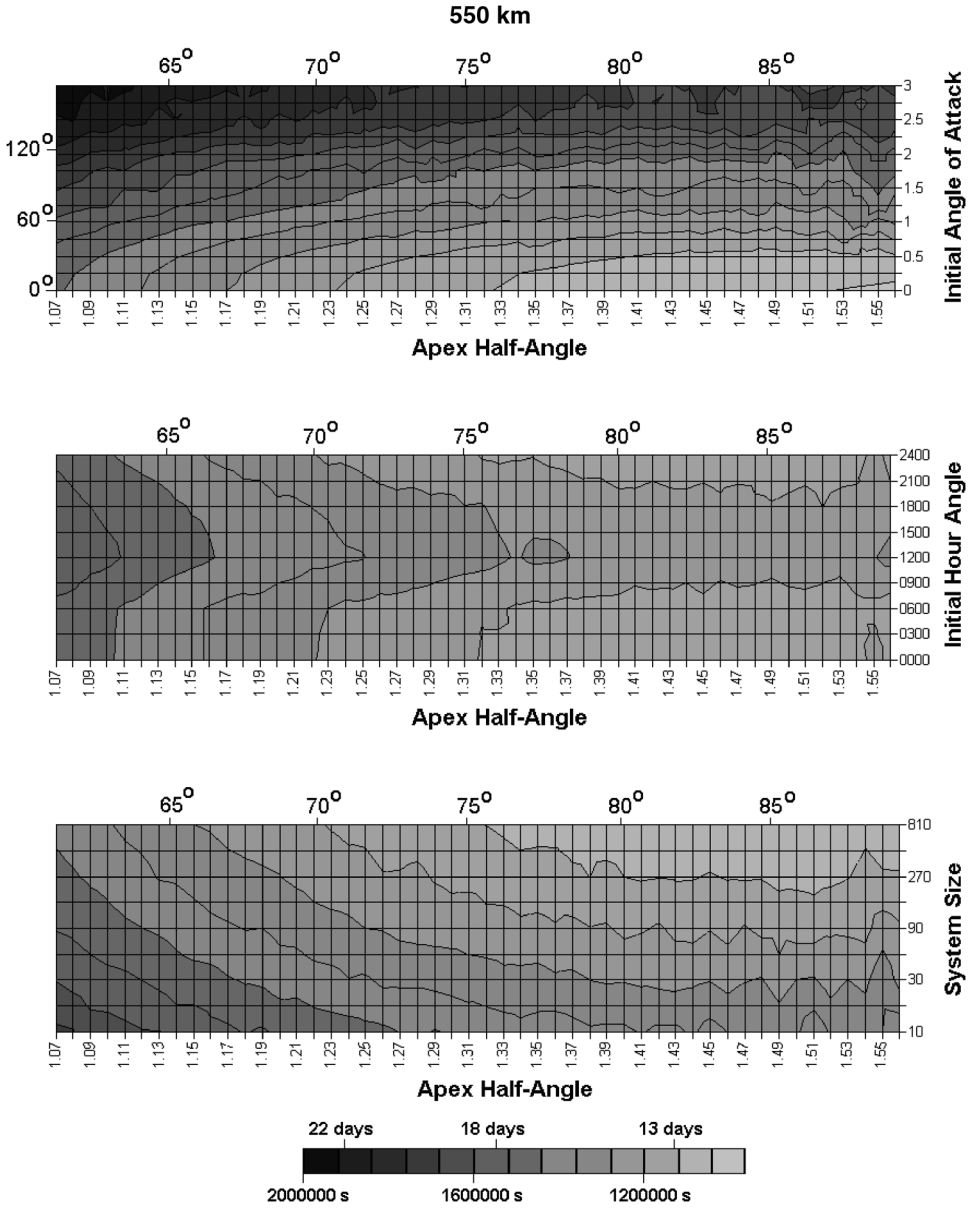

Fig. 6 Average deorbit times (see scale bar) from 550 km, varying with apex half-angle (in radians), initial angle of attack (in radians), initial hour angle (in hours), and system size (in kg and m^2); mass-to-area ratio is reduced by the drag sail to 1 kg/m^2 throughout.

VI. Discussion of the Results of the Deorbit Simulations

A. Effect of the Initial Angle of Attack

It appears that a lower initial angle of attack will result in a faster deorbit time. This can be explained by an examination of Fig. 4a, which indicates that maximum drag is generated when the angle of attack is zero. Because a nonzero angle of attack will result in the oscillatory motion shown in Fig. 8, this will tend to reduce the average aerodynamic drag generated and thus delay deorbit.

B. Effect of the Initial Hour Angle

Deployment between 2000 and 0600 hrs results in a faster deorbit than deployment at any other time, although the effect is considerably weaker than the effect of the initial attack angle.

This result may be explained by again considering Fig. 8, which demonstrates the diurnal variation in the angle of attack. In particular, it is demonstrated that the amplitude of the oscillations of the device increases during the night and diminishes during the day. This trend is associated with the diurnal variation of atmospheric density at altitude, which tends to peak in the early afternoon and trough in the early morning [8].

The manner by which this variation can influence the oscillations of an aerostable structure has been previously discussed [9] and is analogous to a pendulum oscillating in a varying gravity field. If the gravitational acceleration is increased, the oscillations of the bob reduce in amplitude but, to conserve energy, increase in frequency. If the gravity is reduced, the opposite is the case.

Therefore, a deployment near the peak of the diurnal density variation will result in an initial angle of attack that is likely to increase, whereas a deployment near the trough is likely to lead to a reduction. Higher time-averaged angles of attack are likely to prolong deorbit, for the reasons set out in Sec. VI.A.

If the initial angle of attack is sufficiently high and deployment takes place near the peak of the diurnal density cycle, the amplitude-augmenting effects of the diurnal density variation may even be sufficient to induce a tumbling motion, as seen in Fig. 8b.

C. Effect of the Size of the System

Although the mass-to-area ratio of all the systems considered is held constant at 1 kg/m^2, there are considerable differences in scale. As the size of the system increases, the balance between the different aerodynamic quotients will change. In particular, the damping quotient increases at a greater rate than the restoring quotient, which

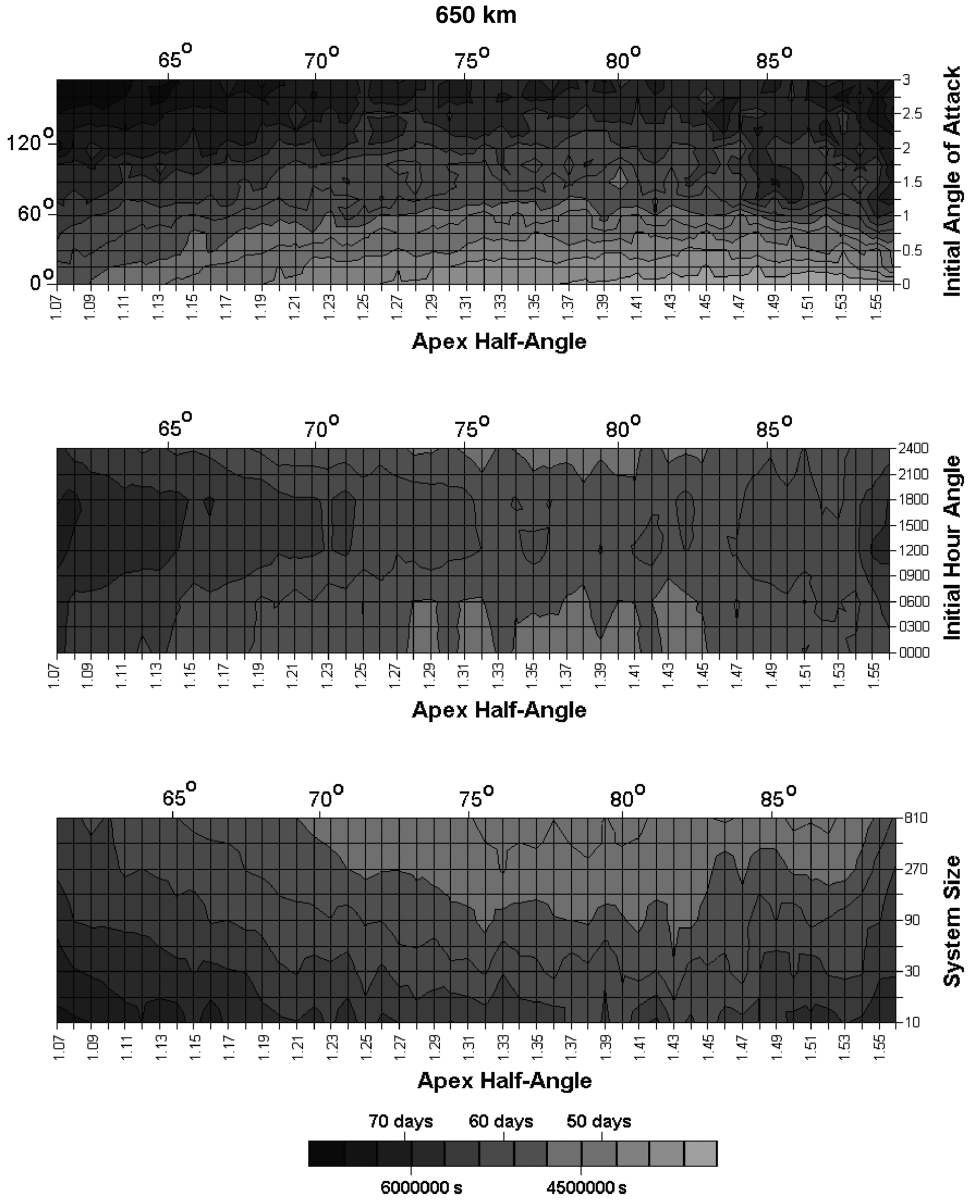

Fig. 7 Average deorbit times (see scale bar) from 650 km, varying with apex half-angle (in radians), initial angle of attack (in radians), initial hour angle (in hours), and system size (in kg and m^2); mass-to-area ratio is reduced by the drag sail to 1 kg/m^2 throughout.

in turn increases faster than the lift and drag quotients. However, the rotational inertia of the spacecraft increases at the greatest rate of all.

These factors combine to make the larger devices oscillate more slowly and be less susceptible to the effects of density variations. Augmentation of attack angle and the development of tumbling motions are therefore impeded and a faster average deorbit time results.

D. Effect of Apex Half-Angle

The optimum apex half-angle appears to vary from 1.55 rad in the case of deorbits from 450 km to 1.5 rad from 550 km and, finally, to 1.4 rad from 650 km. These values represent the tradeoff between the higher stability of sharper conical shapes and the greater drag of blunt conical shapes, with slightly more stability being required to withstand the proportionately more violent diurnal density variations found at higher altitudes.

VII. Reentry Considerations

As was stated earlier, the drag sail must collapse at altitude if maximum aerodynamic heating is to be applied to the host and the maximum amount of material ablated before it reaches the surface. Studies at Cranfield University [10] have shown that a similar device must collapse above 120 km to ensure maximum heating, but other authors [11] have stated that aerodynamic heating is significant as high as 150 km.

To ensure safety on the ground but maintain a good deorbit performance, the deployed structure will be designed to collapse under aerodynamic loads at a maximum altitude of 250 km, but no lower than 150 km.

VIII. Practicality

An aerostable drag-enhancement deorbit device was shown to meet the requirements of [1] and deliver a high-performance deorbit solution, but the practicality of a typical device must still be demonstrated.

First, the architecture of the device and folding of the sails is based on earlier solar-sail/deployable-antenna designs [12] and biomimetic patterns [13] to maximize the packing efficiency of the structure, as shown in Fig. 9.

To provide a mass-efficient solution, the deorbit device must have a mass penalty similar to that required for effective deorbit by alternative means. A logical choice for an acceptable mass limit is the mass of fuel required for a controlled deorbit burn [14]. For a LEO

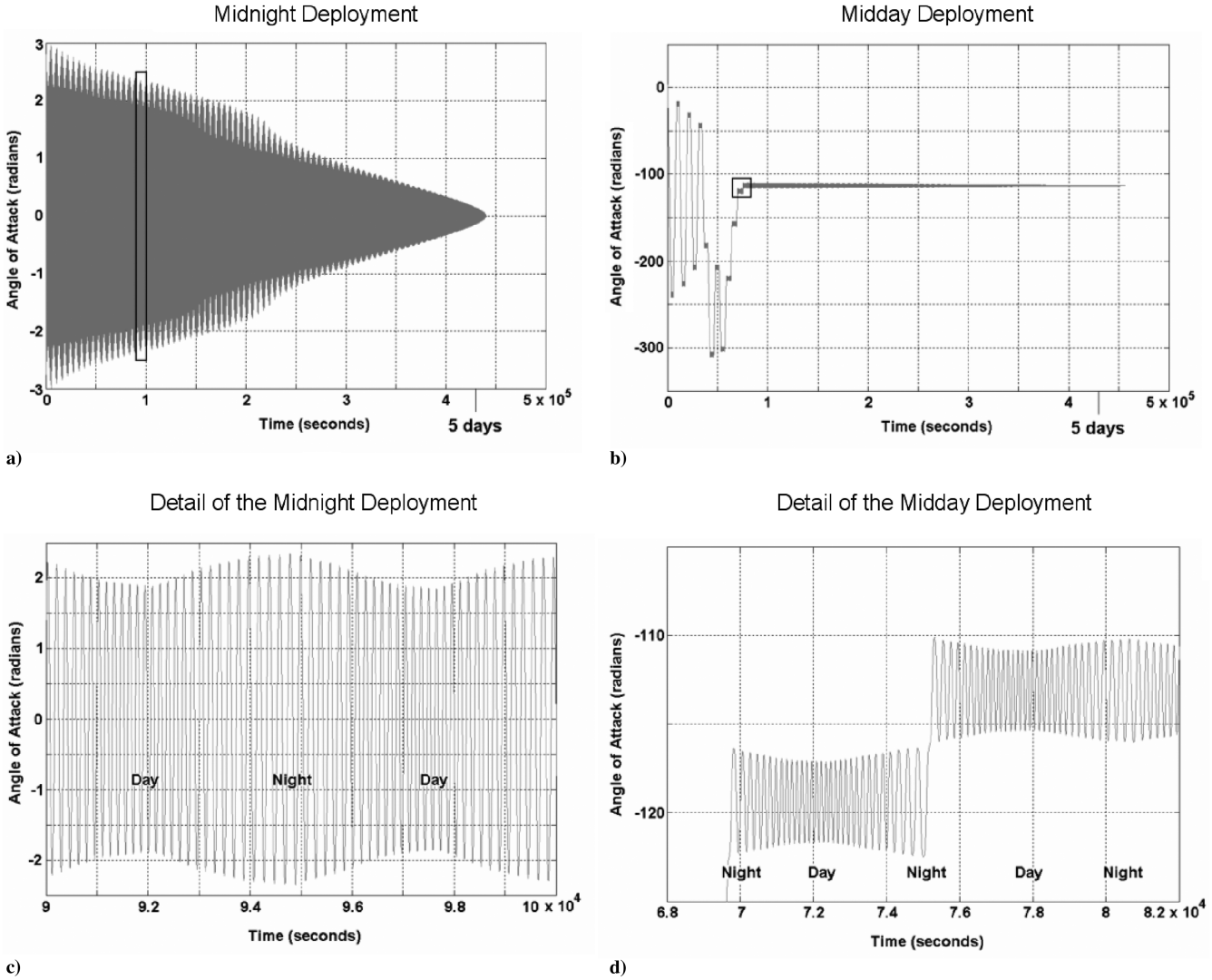

Fig. 8 Angle-of-attack histories produced by 10 kg/10 m^2 systems deorbiting from 450 km, with an initial angle of attack and apex half-angle of 2.8 and 1.3 rad (160 and 74 deg), respectively: a) initial hour angle is 0000 hrs, b) initial hour angle is 1200 hrs; and c–d) expanded details indicated by the boxes in Figs. 8a and 8b, respectively.

spacecraft using a chemical propulsion, this limit is around 5% of the total spacecraft mass in the worst case.

If we take as an example a 200-kg host spacecraft and desire a conservative mass-to-area ratio of 1 kg/m^2, we may determine that four deployable booms, each approximately 10 m long, would be required to support 200 m^2 of drag-sail material. The booms and their canisters would amount to approximately 3 kg if leading commercial systems were used, whereas the drag sail might amount to 10 g/m^2, or 2 kg [15].

If the booms could be collapsed to 2% of their deployed length, the deorbit device would have a planform of approximately 30 cm square and a height of around 15 cm. This volume would require a protective casing that, if it were 1-mm-thick Kevlar epoxy, would amount to 0.4 kg. Meanwhile, the systems (radio kit, actuators, batteries, etc.) would be comparable in terms of mass to those required for CubeSat missions, with an allocation of 0.4 kg in total [16].

The structure of small space systems is typically 20% of the total [17], which, in this case, would be 1.45 kg. With a final 10% contingency, the total mass estimate for the deorbit device rises to 8.06 kg.

This represents 4% of the mass of the host, which places the deployable-drag-sail concept in the acceptable mass range for deorbit systems.

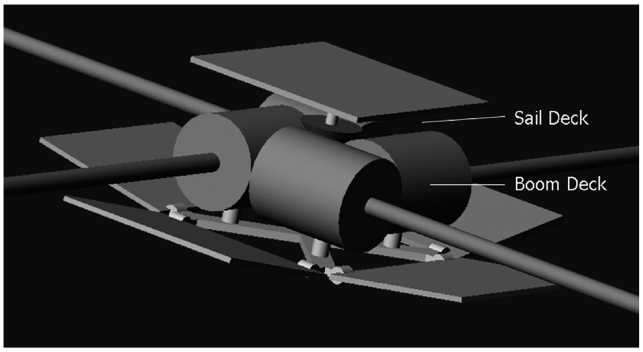

Fig. 9 Conceptual layout of the deorbit device unit; the drag sails are not shown, but the outer casing is shown opened, and the booms are depicted in the deployed state.

IX. Conclusions

Drag-enhancement devices for the deorbit of spacecraft from low Earth orbit were discussed and shown to fulfill NASA guidelines for end-of-life deorbit. The concept is a trailing drag sail that can be deployed from a small package attached to the host at launch. The effectiveness of such a device was demonstrated both in terms of performance and mass efficiency.

The optimum system operating at 650 km will deploy a drag sail with an apex half-angle of approximately 1.4 rad, although this will be slightly increased at low altitudes. Performance can also be increased by deploying at a low initial angle of attack in the late evening or early morning. Offsetting the center of mass forward from the sail apex, as is likely to be the case, will aid the stability further.

Finally, it appears that larger systems are proportionately more effective than small systems operating at the same mass-to-area ratio.

References

[1] "NASA Safety Standard Guidelines and Assessment Procedures for Limiting Orbital Debris," NASA Rept. NSS-1740.14, Aug. 1995.

[2] "Orbital Debris Quarterly News," Vol. 10, No. 2. NASA Orbital Debris Program Office, Johnson Space Center, Houston, TX, Apr. 2006.

[3] Mayer, K. W., and Chao, C. C., "Atmospheric Reentry Disposal for Low-Altitude Spacecraft," *Journal of Spacecraft and Rockets*, Vol. 37, No. 5, 2000, pp. 670–674.

[4] Andringa, J. M., and Hastings, D. E., "A Systems Study on How to Dispose of Fleets of Small Satellites," AIAA Space 2001—Conference and Exposition, Albuquerque, NM, AIAA Paper 2001-4741, 2001.

[5] Petro, A. J., "Techniques for Orbital Debris Control," *Journal of Spacecraft and Rockets*, Vol. 29, No. 2, 1992, pp. 260–263.

[6] Campbell, S., "Orbital Stability and Other Considerations for U. S. Government Guidelines on Post-Mission Disposal of Space Structures," *Proceedings of the Third European Conference on Space Debris*, Vol. 2, SP-473, ESA, Noordwijk, the Netherlands, 2001, pp. 835–839.

[7] Hedin, A. E., "Extension of the MSIS Thermospheric Model into the Middle and Lower Atmosphere," *Journal of Geophysical Research*, Vol. 96, Feb. 1991, p. 1159.

[8] King-Hele, D., *Satellite Orbits in an Atmosphere*, Blackie & Sons, Glasgow, Scotland, 1987.

[9] Kumar, R., "Parametric and Classical Resonance in Passive Satellite Aerostabilization," *Journal of Spacecraft and Rockets*, Vol. 33, No. 2, 1996, pp. 228–234.

[10] Chutha, J., "Deorbit and Atmospheric Entry of Nanosatellites," M.S. Thesis, Cranfield Univ., Cranfield, England, U.K., 2001.

[11] Sessler, A. M., Cornwall, J. M., Dietz, B., Fetter, S., Frankel, S., Garwin, R. L., Gottfried, K., Gronlund, L., Lewise, G. N., Postol, T. A., and Wright, D. C., "The Re-Entry Heating of Submunitions," *Countermeasures*, Union of Concerned Scientists, Cambridge, MA, and Massachusetts Inst. of Technology, Cambridge, MA, Apr. 2000, pp. 149–158.

[12] Unckenbold, W. F., Eiden, M. J., Herbeck, L., Leipold, M., Schoppinger, C., and Sickinger, C., "Boom Deployment Mechanism for Large Deployable Antennas," *25th ESA Antenna Workshop on Satellite Antenna Technology* [CD-ROM], ESA, Paris, 2002; also available at http://www.hps-gmbh.com/index.php?downloads [retrieved 29 Mar. 2007].

[13] Kobayashi, H., Kresling, B., and Vincent, J. F. V., "The Geometry of Unfolding Tree Leaves," *Proceedings of the Royal Society of London, Series B: Biological Sciences*, Vol. 265, No. 1391, 1998, pp. 147–154.

[14] Roberts, P., "Drag Sail Dynamics for End of Life Deorbit (AAS 04-209)," *Advances in the Astronautical Sciences*, Vol. 119, Part 2, 2005, pp. 1663–1676.

[15] Garner, C., Diedrich, B., and Leipold, M., "A Summary of Solar Sail Technology Developments and Proposed Demonstration Missions," NASA Rept. JPC-99-2697, 1999.

[16] Waydo, S., Henry, D., and Campbell, M., "CubeSat Design for LEO Based Earth Science Missions," *2002 IEEE Aerospace Conference Proceedings*, Vol. 1, Inst. of Electrical and Electronics Engineers, Piscataway, NJ, 2002, pp. 435–445.

[17] Shirgur, B., and Shannon, D., "The Design and Feasibility Study of Nanosatellite Structures for Current and Future FSI Micromissions," *Proceedings of the 14th Annual Small Satellite Conference* [CD-ROM], Utah State Univ., Logan, UT, 2000.

A. Ketsdever
Associate Editor